CAMBRIDGE
UNIVERSITY PRESS

Article

Fluoralforsite, Ba$_5$(PO$_4$)$_3$F – a new apatite-group mineral from the Hatrurim Basin, Negev Desert, Israel

Arkadiusz Krzątała[1] (iD), Katarzyna Skrzyńska[1] (iD), Georgia Cametti[2] (iD), Irina Galuskina[1] (iD), Yevgeny Vapnik[3] and Evgeny Galuskin[1] (iD)

[1]Institute of Earth Sciences, Faculty of Natural Sciences, University of Silesia, Będzińska 60, 41-200 Sosnowiec, Poland; [2]Institute of Geological Sciences, University of Bern, Baltzerstrasse 1+3, 3012 Bern, Switzerland; and [3]Department of Geological and Environmental Sciences, Ben-Gurion University of the Negev, POB 653, Beer-Sheva 84105, Israel

Abstract

Fluoralforsite, ideally Ba$_5$(PO$_4$)$_3$F, (space group $P6_3/m$ (#176), Z = 2, a = 10.0031(2) Å, c = 7.5382(2) Å and V = 653.23(3) Å^3), is a new mineral species of the apatite group – a Ba-analogue of fluorapatite and a F-analogue of alforsite. It was discovered in rankinite paralava filling cracks in pyrometamorphic gehlenite hornfels near the tributary of wadi Zohar and Gurim Anticline, Hatrurim Basin, Negev Desert, Israel. Fluoralforsite occurs in small intergranular spaces between large gehlenite and garnet crystals and in enclaves inside large rankinite crystals with other Ba minerals such as walstromite, zadovite, bennesherite, gurimite, mazorite, barioferrite and baryte. It forms tiny transparent, colourless crystals up to 50 μm with a white streak and a vitreous lustre. The cleavage was not observed. It exhibits a brittle tenacity and a conchoidal fracture. The estimated Mohs hardness is 4–4½, and its calculated density is 4.57 g/cm^{-3}. Fluoralforsite is uniaxial (−) with refractive indices (589 nm) n_ω = 1.689(3) and n_ϵ = 1.687(3). The empirical crystal-chemical formula for the holotype calculated on the basis of 8 cations is: (Ba$_{3.81}$Ca$_{0.97}$Na$_{0.07}$K$_{0.05}$Sr$_{0.05}$Fe$_{0.05}$)$_{\Sigma5}$(P$^{5+}_{2.32}$V$^{5+}_{0.29}$S$^{6+}_{0.22}$Si$_{0.17}$)$_{\Sigma3}$O$_{12}$(F$_{0.85}$Cl$_{0.13}$)$_{\Sigma0.98}$. The crystal structure was refined from single-crystal X-ray diffraction data with R_1 = 0.0192. The structural investigation indicated an ordered arrangement of Ba/Ca at the $M1$ site within individual columns running along the c-axis, but a disordered distribution among adjacent columns throughout the structure, which enables the maintenance of the $P6_3/m$ space group. Fluoralforsite was formed at the final stage of crystallisation as a result of a reaction between the primary mineral assemblages and residual melt.

Introduction

The apatite-supergroup minerals can be described by the general formula $^{IX}M1_2^{VII}M2_3(^{IV}TO_4)_3X$ (Z = 2), where the Roman numbers indicate the ideal coordination number; M and T are cationic sites and X is the anionic site. They crystallise in the hexagonal or pseudo-hexagonal system. The structure consists of columns parallel to the c axis made of face-sharing $M1$-centred polyhedra. The coordination number of $M1$ can be divided into six closer and three more distant ligands (oxygens). The closer ones form a metaprism, whereas taking into account the more distant oxygens leads to a tricapped trigonal prism (Henderson *et al.*, 2009; Pasero *et al.*, 2010). The $M1$ columns are connected by corner-sharing tetrahedra (T sites). The six columns of tricapped trigonal prisms combined with tetrahedra form a channel with hexagonal symmetry along the c-axis (Henderson *et al.*, 2009). The inter-column space (channels) is occupied by $M2$ cations and anionic sites (X = Cl, F and OH). The coordination number of $M2$ sites varies

depending on the type of cations and anions at the X site. In the archetype structure (space group $P6_3/m$), $M2$ is seven-fold coordinated – a distorted pentagonal bipyramid (Pasero *et al.*, 2010). Anionic sites lie in the centre of the channel. However, their position along the c-axis depends on the type of adjacent anions and cations (Hughes *et al.*, 1989, 1990).

The high flexibility of the chemical composition characterises the apatite structure-type. Currently, the following elements are mentioned as the species-defining ones: M = Ca^{2+}, Sr^{2+}, Ba^{2+}, Pb^{2+}, Mn^{2+}, Cd^{2+}, Na$^+$, Y^{3+}, La^{3+}, Ce^{3+}, Nd^{3+} and Bi^{3+}; T = P^{5+}, As^{5+}, V^{5+}, Si^{4+}, S^{6+} and B^{3+}; X = F$^−$, (OH)$^−$, Cl$^−$ and O$^{2−}$ (Pasero *et al.*, 2010). Based on chemical and crystal-chemical grounds, the following five mineral groups have been distinguished within the apatite supergroup: apatite group, hedyphane group, belovite group, britholite group and ellestadite group. Among all these groups, the minerals belonging to the apatite group are the most widespread in Nature. This group includes minerals with pentavalent elements at the T site (P, V and As) and containing the same prevailing (species-defining) bivalent cation at the $M1$ and $M2$ sites. Therefore, the simplified formula, $M_5(TO_4)_3X$, is used in literature for this group (Pasero *et al.*, 2010). Most of the apatite-group members crystallise in space group $P6_3/m$. In contrast, the hedyphane group can host different cations at the

$M1$ and $M2$ sites, resulting in various hexagonal and pseudo-hexagonal symmetries. On the other hand, belovite-type minerals crystallise in lower symmetry due to the ordered arrangement of cations at two independent $M1$ sites, $M1$ and $M1'$. $P6_3$ symmetry is characteristic of minerals containing divalent cations at all M sites, and $P\bar{3}$ is characteristic symmetry of minerals containing REE^{3+} and monovalent cations at split $M1$ sites and a divalent cation at the $M2$ site (Pasero et al., 2010; Pekov et al., 2012).

Fluoralforsite, ideally $Ba_5(PO_4)_3F$ is the Ba-analogue of fluorapatite and the F-analogue of alforsite $Ba_5(PO_4)_3Cl$ (Newberry et al., 1981) belonging to the apatite group. It was found in coarse-grained rankinite paralava in the Hatrurim Basin (Negev Desert), Hatrurim Complex in Israel (Fig. 1), which is a well-known source of new minerals, especially Ba species such as zadovite, aradite, gurimite, hexacelsian, bennesherite and mazorite (Galuskin et al., 2015a; Galuskina et al., 2017a; Juroszek et al., 2022; Krzątała et al., 2022). It is the fourth barium phosphate belonging to the apatite supergroup, after alforsite $Ba_5(PO_4)_3Cl$ (apatite group), kuannersuite-(Ce) $NaCeBa_3(PO_4)_3F_{0.5}Cl_{0.5}$, (belovite group) and miyahisaite (Sr, Ca)$_2$Ba$_3$(PO$_4$)$_3$F (hedyphane group; Table 1). The synthetic analogue of fluoralforsite was reported by Mathew et al. (1979). A comparison of the main crystallographic properties of barium apatite-supergroup minerals and synthetic analogues is presented in Table 1.

Fluoralforsite, $Ba_5(PO_4)_3F$, was named according to the Commission on New Minerals, Nomenclature and Classification of the International Mineralogical Association (IMA-CNMNC) recommendations for the new minerals of the apatite supergroup (Pasero et al., 2010; Hatert et al., 2013). The mineral was named by adding the adjectival prefix for the anion, fluor, to the root name, alforsite, giving fluoralforsite. Consequently, the mineral symbol is Fafr.

A small polished fragment of paralava from the tributary of wadi Zohar with grains of fluoralforsite has been deposited in the mineralogical collection of the Natural History Museum of Bern, Bernstrasse 15, CH-3005 Bern, Switzerland, catalogue number 44951. This work provides data about the new mineral and discusses the crystallographic aspects and ordering of cations and anions in detail.

Occurrence and description of fluoralforsite

Fluoralforsite $Ba_5(PO_4)_3F$ was found in coarse-grained rankinite paralava in the Hatrurim Basin (Negev Desert), Hatrurim Complex in Israel (Fig. 1). The unique Hatrurim Complex is composed of pyrometamorphic rocks and their alteration products, which are distributed on both sides of the Dead Sea Transform Fault in Israel, the West Bank, and Jordan (Fig. 2; Gross, 1977; Burg et al., 1991; Geller et al., 2012). The pyrometamorphic rocks were formed as a result of the high-temperature metamorphism of a sedimentary protolith at sanidinite facies (>600°C and low pressure). They are represented mainly by spurrite marble, larnite pseudoconglomerates, gehlenite hornfelses and different types of paralavas (Vapnik et al., 2007; Novikov et al., 2013; Galuskina et al., 2014). In the Hatrurim Basin, the common type of paralava occurs as lenses within the hornfelses mainly composed of gehlenite, andradite and larnite. The lenses range in size from about ten centimetres to a few millimetres. The occurrence of the paralava in hornfels suggests that the high temperature of the pyrometamorphic processes caused partial protolith melting on a local scale. Moreover, rock-forming minerals of coarse-grained paralava contain melt inclusions with 1200–1250°C homogenisation temperature (Sharygin et al., 2006). Andradite–flamite, gehlenite–flamite and walstromite–kalsilite intergrowths are present in the paralava, which also indicate crystallisation of rocks from melt (Gfeller et al., 2015; Krzątała et al., 2020). The characteristic feature of rankinite paralavas is the occurrence of the Ba, V-bearing enclaves, which are a source of new minerals species such as zadovite, $BaCa_6[(SiO_4)(PO_4)](PO_4)_2F$, aradite, $BaCa_6[(SiO_4)(VO_4)](VO_4)_2F$, hexacelsian, $BaAl_2Si_2O_8$, gurimite $Ba_3(VO_4)_2$, bennesherite $Ba_2FeSi_2O_7$, pliniusite $Ca_5(VO_4)_3F$ and mazorite $Ba_3(PO_4)_2$.

Fluoralforsite has been found in the rankinite-rich paralava (the holotype locality 31°11.3'N, 35°16.6'E) from the upper reaches of the tributary of the wadi Zohar. Additionally, it was found in a paralava sample from Gurim Anticline (Fig. 2). It occurs in small enclaves in association with the following Ba-minerals: walstromite, zadovite–aradite series, gurimite, bennesherite, barioferrite and baryte (Fig. 3). The rock-forming minerals of those paralava are mainly represented by rankinite,
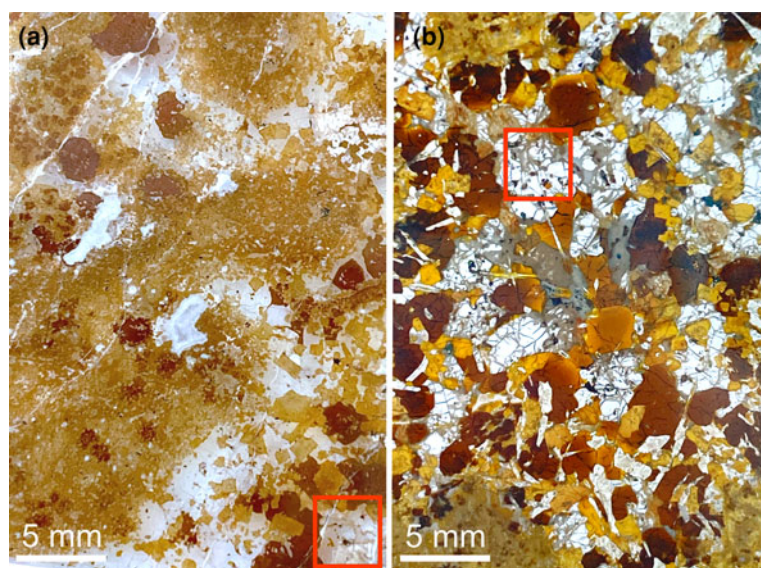

Figure 1. Samples of rankinite paralava from (a) wadi Zohar tributary and (b), Gurim Anticline Hatrurim Basin, in which fluoralforsite was found. The areas framed by red rectangles in (a) and (b) are magnified in Figs 3a,b and 3e,f, respectively. The main minerals of this paralava are distinguished by colour: Ti-rich andradite is brown to black, melilite of the gehlenite–alumoåkermanite series is brown to yellow-light brown, rankinite, fluorapatite, kalsilite and cuspidine are pale pink, light-grey or colourless, secondary Ca-hydrosilicates are chalk white or beige.

Table 1. Comparison of the structural and physical properties of fluoralforsite with selected minerals of the apatite supergroup and synthetic Ba$_5$(PO$_4$)$_3$F.

Mineral species	Fluoralforsite (this study)	Alforsite (Newberry et al., 1981)	Kuannersuite-(Ce) (Friis et al., 2004)	Fluorstrophite (Klevtsova, 1965)	Miyahisaite (Nishio-Hamane et al., 2012)	Synthetic (Mathew et al., 1979)
End-member	Ba$_5$(PO$_4$)$_3$F	Ba$_5$(PO$_4$)$_3$Cl	NaCeBa$_3$(PO$_4$)$_3$F$_{0.5}$Cl$_{0.5}$	SrCaCa$_3$(PO$_4$)$_3$F	(Sr,Ca)Ba$_3$(PO$_4$)$_3$F	Ba$_5$(PO$_4$)$_3$F
Group assignment	apatite	apatite	belovite	belovite	hedyphane	–
Space group	$P6_3/m$	$P6_3/m$	$P\bar{3}$	$P6_3$	$P6_3/m$	$P6_3/m$
Cell parameters						
a (Å)	10.0031(2)	10.25(1)	9.9097(6)	9.63	9.921(2)	10.153(2)
c (Å)	7.5382(2)	7.64(2)	7.4026(6)	7.22	7.469(3)	7.733(1)
Volume (Å^3)	653.23(3)	700.66	629.56	579.86	636.7	690.35
Density (g/cm^3)	4.566 (calc.)	4.83(2)	4.51(1) (calc.)	3.705	4.511 (calc.)	4.76 (calc.)
Optical sign	(−)	(−)	(−)	–	(−)	–
ω	1.689(3)	1.70(1)	1.694(1)		1.669	
ε	1.687(3)	1.70(1)	1.669(1)		1.658	

Ti-rich andradite, members of the gehlenite–alumoåkermanite series, members of the fluorapatite–fluorellestadite series, kalsilite and wollastonite (Fig. 3). Additionally, the following minerals occur in the association: pliniusite, fresnoite, celsian, members of the magnetite–magnesioferrite–trevorite series, U–Nb-bearing cuspidine, nepheline, native copper and hashemite. The paralava voids are filled by low-temperature mineralisation represented by zeolites, afwillite and tobermorite-like Ca-hydrosilicates.

The crystals of fluoralforsite are colourless and transparent up to 50 μm in length and characterised by a white streak and a vitreous lustre. The cleavage is not observed. The tenacity is brittle and the fracture is uneven. Fluoralforsite is uniaxial (−) with refractive indices (589 nm) $n_\omega = 1.689(3)$ and $n_\varepsilon = 1.687(3)$. Based on the average chemical composition and unit cell parameters, the calculated density is 4.57 g/cm^3. Micro-hardness measurements gave a mean VHN$_{25}$ value of 320.4 kg/mm^2 (ranging from 301 to 340 kg/mm^2) based on 12 measurements. This value corresponds to a Mohs hardness of ca. 4–4½.

Experimental methods

The morphology and composition of the minerals were studied using optical microscopy, a scanning electron microscope (Phenom XL and FEI Quanta 250, Institute of Earth Science, Faculty of Natural Sciences, University of Silesia in Katowice, Poland) and an electron microprobe analyser (EMPA, Cameca SX100, Institute of Geochemistry, Mineralogy and Petrology, University of Warsaw). Chemical analyses were carried out (wavelength dispersive spectroscopy mode, 15 kV, 10 nA and ~1 μm beam diameter) using the following lines and standard materials: F$K\alpha$ – synthetic fluorophlogopite; Cl$K\alpha$ – sodalite; Na$K\alpha$ – albite; Si$K\alpha$ and Ca$K\alpha$ – diopside; K$K\alpha$ – orthoclase; Fe$K\alpha$ – Fe$_2$O$_3$; Ba$L\alpha$ and S$K\alpha$– baryte; Sr$L\alpha$ – celestine; V$K\alpha$ – V$_2$O$_5$; and P$K\alpha$ – YPO$_4$.

The Raman spectra of fluoralforsite were recorded on a WITec alpha 300R Confocal Raman Microscope (Institute of Earth Science, Faculty of Natural Sciences, University of Silesia in Katowice, Poland) equipped with an air-cooled solid-state laser (488 nm) and a CCD camera operating at −61°C. The laser radiation was coupled with a microscope through a single-mode optical fibre with a diameter of 3.5 μm. An air Zeiss LD EC Epiplan-Neofluan DIC−100/0.75NA objective was used. Raman scattered light was focused on a broadband single-mode fibre with an effective pinhole size of ~30 μm and a monochromator with a 600 mm^{-1} grating. The power of the laser at the sample position was ~40 mW. An integration time of 5 s, an accumulation of 20 scans and a resolution of 3 cm^{-1} were chosen. The monochromator was calibrated using the Raman scattering line of a silicon plate (520.7 cm^{-1}). Spectra processing, such as baseline correction and smoothing, was performed using the SpectraCalc software package *GRAMS* (Galactic Industries Corporation, NH, USA). Band fitting was performed using a Gauss–Lorentz cross-product function, with a minimum number of component bands used for the fitting process.

Single-crystal X-ray diffraction data were collected with ω scans at different phi-kappa-theta settings using a four-circle Rigaku Synergy R diffractometer (University of Bern, Switzerland), equipped with a PhotonJet-R source, featuring a Mo-rotating anode (Mo$K\alpha$ = 0.71073 Å) and a Hypix Arc 100° detector. The measurement was carried out at room temperature. The investigated sample consisted of a grain (∼0.05 × 0.04 × 0.03 mm) from the wadi Zohar tributary. The analysis of the collected reflections showed that the selected grain consisted of several phases. Approximately 40% of the total reflections were indexed with a
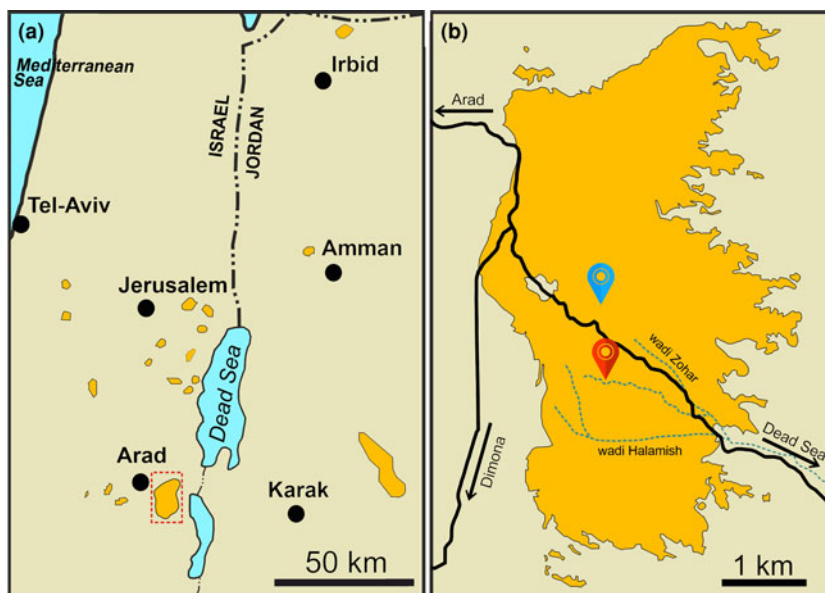
Figure 2. (a) Schematic map of the Middle East with outcrops of pyrometamorphic rocks of the Hatrurim Complex (dark yellow). The framed part is magnified in b. (b) Schematic map of the Hatrurim Basin. The sampling areas of rankinite paralava are marked by a red pin (an unnamed tributary of wadi Zohar) and a blue pin (Gurim Anticline) (modified after Britvin et al., 2015).

hexagonal unit cell: $a = 10.00$ Å, $c = 7.54$ Å; $V = 654$ Å^3, corresponding to fluoralforsite. The second set of reflections ($\sim$30%) was indexed by the rhombohedral cell $a = 7.083$ Å, $c = 25.498$ Å; and $V = 1107.5$ Å^3, ascribed to the mineral zadovite (BaCa$_6$[(SiO$_4$)(PO$_4$)](PO$_4$)$_2$F; $R\bar{3}m$; $a = 7.097$ Å and $c = 25.73$ Å) (Galuskin et al. 2015b). No specific phase could be identified in the remaining diffraction spots. Experimental details are summarised in Table 2. The data processing was performed using the software package *CrysalisPro 42.89a*. The data reduction was carried out by using an empirical absorption correction. The fluoralforsite structure was solved in the $P6_3/m$ space group by direct methods using the software *SHELXS* (Sheldrick, 2008) and then refined using *SHELXL* (Sheldrick, 2015) in the *WinGX* package (Farrugia, 2012). The crystallographic information file has been deposited with the Principal Editor of *Mineralogical Magazine* and is available as Supplementary material (see below). Nevertheless, the integration, solution, and refinement attempts were carried out for test purposes in the following space groups $P6_3$, $P\bar{3}$, and $P2_1/m$ (Supplementary Tables S1–S6). All of them converged to inferior to $P6_3/m$ refinement. For better comparison with literature data, the final structural model was refined by using the atomic coordinates reported by Hata et al. (1979) for alforsite ($P6_3/m$).

Chemical composition

The empirical formulas of fluoralforsite were calculated on the basis of 8 cations (Table 3). The following crystal chemical formulas have been obtained on the crystals from the wadi Zohar tributary and Gurim Anticline locality, respectively: (Ba$_{3.81}$Ca$_{0.97}$Na$_{0.07}$K$_{0.05}$Sr$_{0.05}$Fe$_{0.05}$)$_{\Sigma5}$(P$_{2.32}^{5+}$V$_{0.29}^{5+}$S$_{0.22}^{6+}$Si$_{0.17}^{4+}$)$_{\Sigma3}$O$_{12}$(F$_{0.85}$Cl$_{0.13}$)$_{\Sigma0.98}$ (Ba$_{3.92}$Ca$_{0.88}$Na$_{0.08}$K$_{0.02}$Sr$_{0.11}$)$_{\Sigma5.01}$(P$_{2.17}^{5+}$V$_{0.41}^{5+}$S$_{0.23}^{6+}$Si$_{0.11}^{4+}$Al$_{0.07}$)$_{\Sigma2.99}$O$_{12.02}$(F$_{0.92}$Cl$_{0.02}$)$_{\Sigma0.94}$. The analyses of fluoralforsite crystals reveal a significant substitution of Ca^{2+}, nearly equal to one apfu. Thus, the simplified and ideal formula can be written as (Ba,Ca)$_2$Ba$_3$(PO$_4$)$_3$F and Ba$_5$(PO$_4$)$_3$F, respectively.

Raman investigation

The Raman spectra of phosphate minerals of the apatite group are characterised by strong ν_1 symmetric stretching vibrations of (PO$_4$)$^{3-}$ tetrahedra at 950–990 cm^{-1}. The weak bands of ν_2 symmetric bending vibrations, ν_3 antisymmetric stretching vibrations and ν_4 antisymmetric bending vibration are observed in 400–500 cm^{-1}, 1000–1150 cm^{-1} and 550 and 660 cm^{-1} regions, respectively. Bands below 300 cm^{-1} are related to the lattice vibrations (Litasov and Podgornykh, 2017). In the Raman spectra of fluoralforsite (Fig. 4), the main band of (PO$_4$)$^{3-}$ groups vibrations occur at $\sim$942/941 cm^{-1}. The bands at $\sim$410–430 cm^{-1} are related to ν_2 symmetric bending vibrations. The weak bands at $\sim$1008–1048 cm^{-1} can be assigned to ν_3(PO$_4$)$^{3-}$ antisymmetric stretching vibrations, whereby ν_4 antisymmetric bending vibration occurs at $\sim$550–590 cm^{-1} (Levitt and Condrate, 1970; Meegoda et al., 1999). The bands at 840/830 cm^{-1} can be attributed to asymmetric stretching vibrations (ν_3) of VO$_4^{3-}$ or symmetric stretching vibration (ν_1) of SiO$_4^{4-}$ (Schulte et al., 1995; Comodi et al., 1999; Frost et al., 2011; Galuskin et al., 2015b). Low-intensity bands at $\sim$995/991 cm^{-1} can be assigned to the vibrations of (SO$_4$)$^{2-}$ groups. The bands from moderate to weak intensity in the 80–250 cm^{-1} region can be connected with lattice or Ba(Ca)–O modes. The remaining bands in the Raman spectrum of fluoralforsite from both localities and their assignments are [cm^{-1}]: 349, 365/350 (ν_2VO$_4^{3-}$), 379/385 (ν_4VO$_4^{3-}$), 625/626 (ν_4SO$_4^{2-}$), 840/830 (ν_3VO$_4^{3-}$ or ν_1SiO$_4^{4-}$), 860/857 (ν_1VO$_4^{3-}$), 995/991 (ν_1SO$_4^{2-}$) (Fig. 4). Accurate band assignment in the Raman spectra of fluoralforsite is hampered by overlapping bands corresponding to vanadate, sulfate and silicate anionic-group vibrations. The spectra analysis from 3600 cm^{-1} to 3700 cm^{-1} indicates the absence or very low content of hydroxyl groups in the fluoralforsite channel.

X-ray crystallography and structure refinement

The structure of fluoralforsite was solved and refined in space group $P6_3/m$. During the first refinement cycles, $M1$, $M2$ and tetrahedral ($P1$) sites were located (Table 4). Initially, $M1$ and $M2$ sites and tetrahedral position ($P1$) were refined using barium and phosphorus scattering curves, respectively. The next refinement cycle allowed for the location of the anion position (F site, Wyckoff position $4e$), which was refined with fluorine scattering factors. However, a strong peak in the difference-Fourier maps was observed along the c-axis at 1.0 Å from the F site.
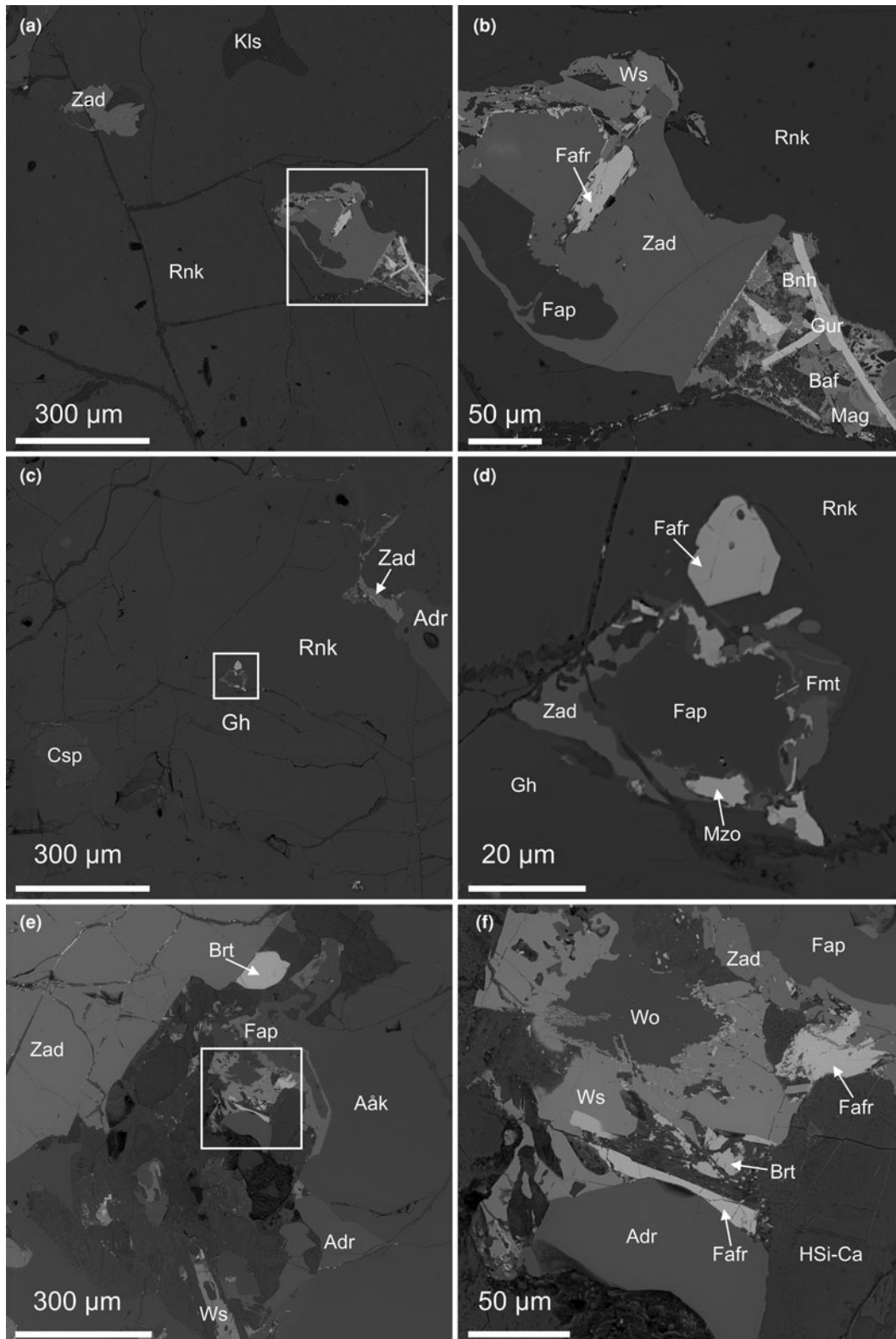
Figure 3. Back-scattered electron (BSE) images of fluoralforsite in paralava near the wadi Zohar tributary (a–d) and Gurim Anticline (e,f). Crystals of fluoralforsite occur between rock-forming minerals in small enclaves enriched in barium. The white frames correspond to the magnified fragments shown on the right side. Mineral abbreviations after Warr (2021): Aåk – alumoåkermanite, Adr – andradite, Baf – barioferrite, Bnh – bennesherite, Brt – baryte, Csp – cuspidine, Fafr – fluor-alforsite, Fap – fluorapatite, Fmt – flamite, Gh – gehlenite, Gur – gurimite, HSi-Ca – hydrosilicate of calcium, Kls – kalsilite, Mag – magnetite, Mzo – mazorite, Rnk – rankinite, Wo – wollastonite, Ws – walstromite, Zad – zadovite.

Table 2. X-ray data collection and crystal structure refinement parameters of fluoralforsite.

Crystal data	
Refined chemical formula	$Ba_4Ca_{0.995}(P_{2.80}V_{0.20})O_{12}(F_{0.845}Cl_{0.11})$
Empirical formula	$Ba_{4.03}Ca_{0.97}(P_{2.32}V_{0.29}S_{0.22}Si_{0.17})_{\Sigma3}O_{12}(F_{0.85}Cl_{0.13})_{\Sigma0.98}$
Crystal system	Hexagonal
Space group	$P6_3/m$ (n. 176)
Unit cell dimensions (Å)	$a = 10.0031(2)$
	$c = 7.5382(2)$
Volume (Å³)	653.23(3)
Z	2
Formula weight	1796.20
Density (calculated) (g/cm³)	4.566
Crystal size (mm)	0.05×0.04×0.03
Data collection	
Diffractometer	Rigaku XtaLAB, Synergy R
Radiation wavelength (Å)	0.71073
Detector-to-sample distance (mm)	50
Temperature (K)	293(2)
Total time/Dose time	1h 18m/ 1h 16m
$F(000)$	792
θ range for data collection (°)	2.351–35.064
Index ranges	$-15 \leq h \leq 15$
	$-15 \leq k \leq 16$
	$-11 \leq l \leq 12$
Reflections collected	17362
Independent reflections	1009
Observed Data ($I > 2\sigma(I)$)	890
R_{int} and R_{sigma}	0.0542 and 0.0194
Refinement	
No. of parameters	64
No. of restraints	0
Weighting scheme	$w = 1/(\sigma^2(F_o^2) + (0.0172P)^2 + 0.4911P)$
	where $P = (F_o^2 + 2F_c^2)/3$
R_1 / wR_2 ($I > 2\sigma(I)$)	0.0192/0.0394
R_1 / wR_2 (for all)	0.0242/0.0405
GooF	1.074
$\Delta\rho_{min}$ ($e/Å^3$) close to	-0.67 at 1.46 Å from O3A
$\Delta\rho_{max}$ ($e/Å^3$) close to	0.86 at 0.43 Å from F1

Table 3. Chemical data (in wt. %) of fluoralforsite from wadi Zohar tributary and Gurim Anticline*.

	Wadi Zohar tributary			Gurim Anticline		
	Mean ($n = 7$)	S.D.	Range	Mean ($n = 6$)	S.D.	Range
F	1.82	0.25	1.42–2.22	1.94	0.07	1.86–2.08
Cl	0.53	0.28	0.18–0.67	0.07	0.04	0.02–0.13
Na_2O	0.23	0.06	0.11–0.33	0.27	0.08	0.13–0.37
K_2O	0.25	0.12	0.09–0.41	0.12	0.01	0.10–0.14
CaO	6.16	0.21	5.79–6.52	5.50	0.39	5.11–6.34
SrO	0.56	0.19	0.31–0.99	1.24	0.08	1.17–1.39
BaO	65.42	0.95	63.95–67.01	67.55	1.48	65.45–69.66
FeO	0.39	0.06	0.30–0.46	n.d.	n.d.	n.d.
Al_2O_3	n.d.	n.d.	n.d.	0.38	0.02	0.35–0.42
SiO_2	1.24	0.61	0.32–1.89	0.71	0.04	0.67–0.80
P_2O_5	18.48	1.16	17.34–20.40	16.98	0.49	16.15–17.59
V_2O_5	2.92	0.44	2.24–3.43	4.15	0.30	3.80–4.63
SO_3	1.93	0.46	1.14–2.33	2.03	0.11	1.85–2.17
O=F+Cl	0.88			0.83		
Total	98.62			100.16		
Calculated on 8 cations						
Na^+	0.07			0.08		
K^+	0.05			0.02		
Ba^{2+}	3.81			3.92		
Ca^{2+}	0.97			0.88		
Sr^+	0.05			0.11		
Fe^{2+}	0.05			-		
Sum M	5.00			5.01		
Al^{3+}	-			0.07		
Si^{4+}	0.17			0.11		
P^{5+}	2.32			2.17		
V^{5+}	0.29			0.41		
S^{6+}	0.22			0.23		
Sum T	3.00			2.99		
F	0.85			0.92		
Cl	0.13			0.02		
Sum X	0.98			0.94		

*Note: S.D. – standard deviation; n.d. – not detected.

This residual electron density was modelled as a low-occupied site ($2b$ position), corresponding to the Cl position in alforsite (Table 4; Hata *et al.* 1979; Newberry *et al.*, 1981). In order to model the residual electron density close to the F site, a new low-occupied site F1 (at ~0.6 Å from F) was inserted in the model. Similarly, the residual peak close to $M2$, was modelled by an additional site, $M2A$, refined with barium scattering factors (Tables 4, 5). A calculation of the mean electron number of the $M1$ site gave values of 38.56 e^-, indicating the significant substitution of a lighter cation. Owing to the complex chemistry of the crystal investigated, $M1$ and $P1$ sites were described with mixed scattering curves according to the chemical microanalyses. $M1$ occupancy was refined with Ba vs. Ca curves and finally converged to 0.501(3) Ba and 0.498(3) Ca. The tetrahedral position was refined using a constrained mixed-scattering curve (2.8 P + 0.2 V). The refined site-scattering values are compatible with the chemical formula calculated from the EMPA data (Tables 2, 3). The location of Ca at the $M1$ position is in agreement with the suggestion of Pasero and co-authors guidelines for the apatite supergroup, according to which smaller cations fill the $M1$ site and larger cations the $M2$ site (Pasero *et al.*, 2010). All sites, except low-occupied Cl, F, F1 and $M2A$, were refined using anisotropic displacement parameters (Table 5). The pronounced displacement of O3 was modelled by splitting the site over O3 and

O3A ($12i$ positions) positions, 0.5 Å apart (Table 4, Table 5). The O2 site was located at the $12i$ position, whereas O1 was at the $6h$ special position. The final R-value converged to 1.92% for 1009 unique reflections and 64 refined parameters.

Structure description

Fluoralforsite has an apatite structure type and crystallises in the space group $P6_3/m$ with the following unit cell parameters: $a = 10.0031(2)$, $c = 7.5382(2)$ Å and $V = 653.23(3)$ Å³ (Table 2). The $M1$ site, building columns along the c-axis, is occupied equally by Ba and Ca (Figs 5, 6). The $M1-O$ bond distances vary from 2.60Å ($M1-O1$) to 2.90Å ($M1-O3$). It is worth noting that two different $M1-O2$ bond distances (2.40Å and 2.79 Å) result as a consequence of the O2 position, which is shifted with respect to the mirror plane. However, the two equivalent O2 positions (at z and $-z + ½$) cannot be simultaneously present in the coordination sphere of $M1$ (Table 6, Fig. 6). Hence, the nine-fold coordination is maintained, similar to the archetype structure (Table 6). As mentioned above, the O2 site lies slightly above the mirror plane ($z = 0.21$, Table 4), resulting in two possibilities of tetrahedra tilting (Fig. 5b). The tetrahedron connecting $M1$ columns, is occupied mainly by phosphorus with slight impurities of vanadium. The average $<T-O>$ bond distance is 1.55Å, as for the pure phosphorus tetrahedron (Mathew *et al.*, 1979; Newberry *et al.*, 1981). This value also agrees with the
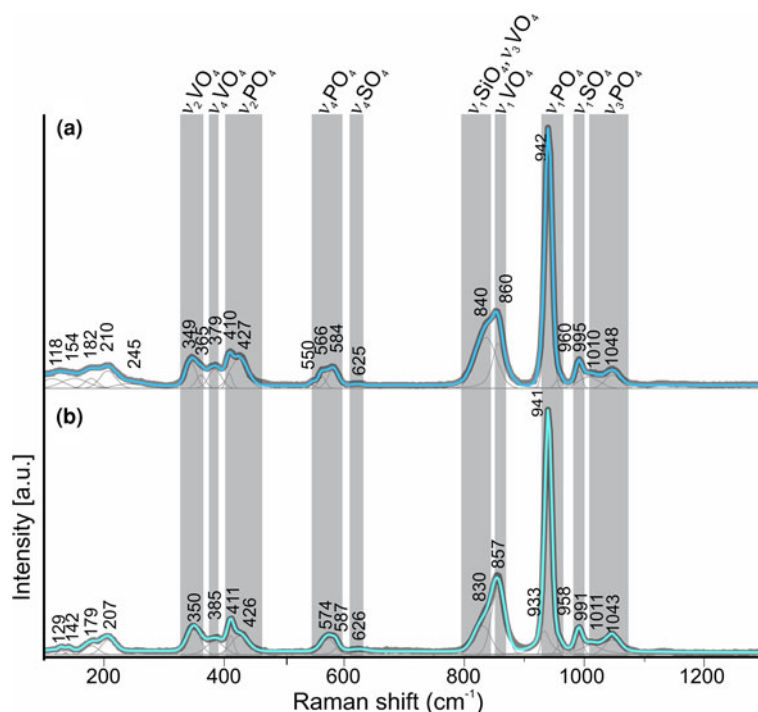
Figure 4. The Raman spectrum of fluoralforsite from (a) the type locality and (b) Gurim Anticline Hatrurim Basin, Hatrurim Complex, Israel.

Table 4. Atom coordinates, equivalent isotropic or isotropic (*) displacement parameters and site occupancies of fluoralforsite.

Site	Atom	x	y	z	$U_{eq}/U_{iso}{}^*$ (Å^2)	Occupancy
M2	Ba	0.23502(3)	0.25414(3)	¼	0.01870(19)	0.925(6)
M2A	Ba	0.2304(16)	0.2457(18)	0.288(5)	0.113(11)*	0.037(3)
M1	Ba	0.3333	0.6667	−0.00237(4)	0.01868(10)	0.501(3)
	Ca	0.3333	0.6667	−0.00237(4)	0.01868(10)	0.498(3)
P1	P	0.40736(8)	0.02868(8)	¼	0.01743(16)	0.934
	V	0.40736(8)	0.02868(8)	¼	0.01743(16)	0.066
O1	O	0.3587(3)	−0.1442(3)	¼	0.0424(7)	1
O2	O	0.5839(3)	0.1282(3)	0.2143(4)	0.0254(10)	0.5
O3	O	0.360(2)	0.0809(17)	0.0813(11)	0.031(2)	0.71(6)
O3A	O	0.306(4)	0.043(3)	0.102(2)	0.022(3)	0.29(6)
Cl	Cl	0	0	0	0.041(6)*	0.112(10)
F	F	0	0	−0.111(3)	0.028(4)*	0.235(18)
F1	F	0	0	−0.193(3)	0.031(5)*	0.185(17)

estimated bond distance (1.56 Å) considering the V, S and Si substitutions at the $P1$ site, as shown by chemical analyses (Nyfeler and Armbruster, 1998; Hawthorne et al., 2000; Baikie et al., 2014). The cation position in the inter-column space is partially disordered along the c-axis and split over two barium sites, $M2$ (Occupancy 0.93) and $M2A$ (Occ. 0.037) (Table 4; Fig. 7). The channel contains three partially occupied anionic sites (Fig. 5c).

Fluorine occupies two $4e$ positions, F and F1, respectively. In turn, the $2b$ position is a low-occupied (Occ. = 0.112(10)) Cl site corresponding to the Cl position in the alforsite (Fig. 7; Hata et al., 1979; Newberry et al., 1981). The anionic arrangement is described in detail in the discussion session.

Discussion

The a unit-cell parameter of fluoralforsite varies considerably compared to that of alforsite, though only slightly from the synthetic phase $Ba_5(PO_4)_3F$ (Table 1; Mathew et al., 1979; Newberry et al., 1981). The difference in the a parameter between fluoralforsite and alforsite may be ascribed to the different radii of the cations (i.e. Ba and Ca) at the $M1$ site. Similarly, the average bond distances of the tricapped trigonal prism for the investigated fluoralforsite ($<M1-O> = 2.59$ Å; Table 6) are significantly shorter than those in alforsite ($<M1-O> = 2.83$ Å), as a result of Ca^{2+} substitution at the $M1$ position. Due to the displacement of the O2 position off the mirror plane, two variants of $M1$ coordination are possible (Fig. 6a). In the first version, the $M1-O2$ bond distance is equal to 2.79 Å. In that case, the $M1$ position is preferentially occupied by Ba^{2+}. In the second variant, the $M1-O2$ distance is equal to 2.40 Å and the cationic position is occupied by Ca^{2+}. As a result, an ordered arrangement within individual

Table 5. Anisotropic displacement parameters (Å^2).

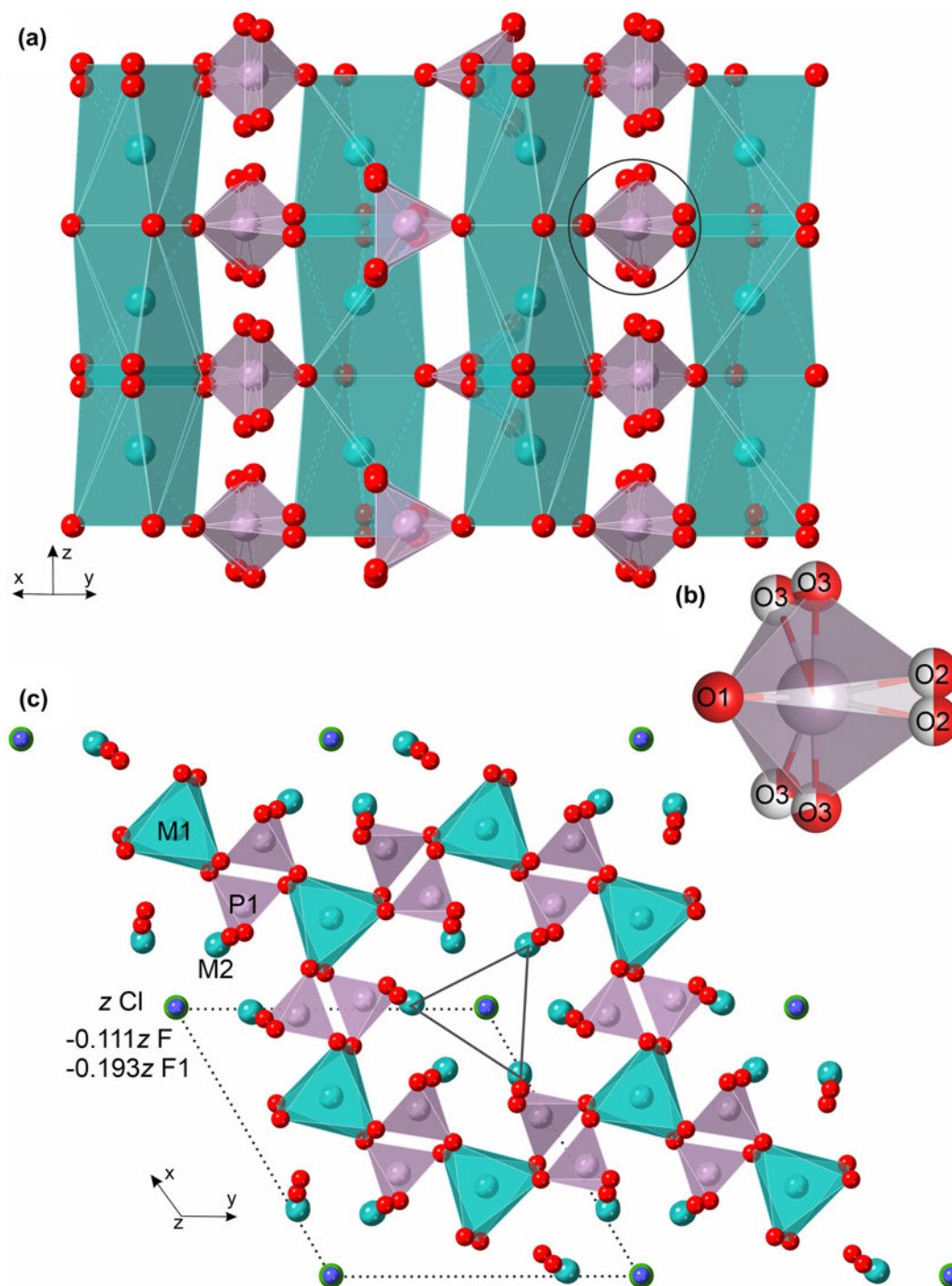| Site	U^{11}	U^{22}	U^{33}	U^{23}	U^{13}	U^{12}
M2	0.02027(19)	0.02244(19)	0.0178(2)	0	0	0.01398(11)
M1	0.01884(12)	0.01884(12)	0.01836(16)	0	0	0.00942(6)
P1	0.0143(3)	0.0135(3)	0.0247(4)	0	0	0.0071(2)
O1	0.0377(16)	0.0202(12)	0.071(2)	0	0	0.0156(12)
O2	0.0179(11)	0.0227(13)	0.033(3)	−0.0024(12)	0.0036(11)	0.0083(10)
O3	0.034(6)	0.038(3)	0.0240(16)	−0.0050(18)	−0.004(2)	0.021(4)
O3A	0.015(7)	0.029(6)	0.020(3)	−0.002(3)	0.000(4)	0.010(6)

Figure 5. (a) Arrangement of *M*1 and P polyhedra in the crystal structure of fluoralforsite projected along [110]. *M*2 and anionic sites are not shown for the sake of clarity. The circle marks the part magnified in b; (b) phosphorus tetrahedron with split O2 and O3 sites; (c) crystal structure of fluoralforsite projected along [001]. The triangle highlights the part of the structure magnified in Fig. 7. Turquoise and light violet polyhedra represent the *M*1 prism and P tetrahedra, respectively. *M*2 sites are shown as a turquoise sphere, red spheres correspond to oxygens and dark blue and green spheres represent fluorine and chlorine, respectively. The dotted line indicates the unit cell. Drawn using *CrystalMaker*® software.

columns should take place (Fig. 6b). Assuming the cations are ordering at *M*1, the symmetry would lower to $P6_3$, similar to fluorcaphite and fluorstrophite (belovite group) or even to $P\bar{3}$ such as in kuannersuite-(Ce) and hydroxylhedyphane (Table 1; Friis *et al.*, 2004; Pekov *et al.*, 2010; Biagioni *et al.*, 2019). Monoclinic symmetry is also probable, such as in pure synthetic hydroxyl- and chlorapatite, where anionic column ordering results in a double *b* unit cell parameter (Hughes and Rakovan, 2002; Pasero *et al.*, 2010). However, in fluoralforsite the $P6_3/m$ symmetry is maintained due to different ordering of Ca/Ba among adjacent columns. The mirror plane at ¼ and ¾ *z* would be lost if there were likewise ordering in adjacent columns. The
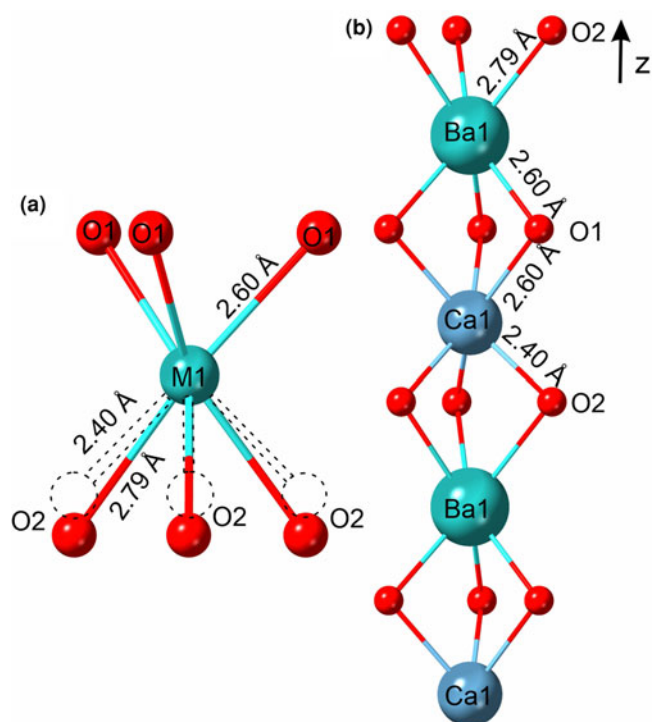
Figure 6. (a) Two variants of an *M*1 metaprism coordinated by O1 and O2, displaced off the mirror plane; (b) ordered *M*1 column arrangement along [001]. The radii proportions of Ca/Ba have been preserved. Drawn using *CrystalMaker*® software.

possibility of different space groups ($P6_3$, $P\bar{3}$, and $P2_1/m$) were tested (Supplementary Tables S1–S6); however, no indication of ordering at the two symmetry-independent *M*1 and *M*1' sites was observed.

In fluoralforsite, tilting of *M*1 polyhedra is caused by the displacement of the O1–O2 edge off the mirror plane (Fig. 5b), whereas in kuannersuite-(Ce) ($P\bar{3}$, belovite group) and hydroxyl-hedyphane ($P\bar{3}$, hedyphane group) a displacement off the polyhedra edge parallel to *c* was observed. We consider that the tilting is related to anions or *M*1-cations ordering (Friis *et al.*, 2004; Biagioni *et al.*, 2019). In fluoralforsite, the O2 sites are shifted from the unique position (.*m*) in order to obtain a favourable bond distance with the large Ba cation and the smaller Ca

Table 6. Selected interatomic distances (Å).

|			
P1–O1	1.544(3)	*M*1–O1	2.6048(17) ×3
P1–O2	1.557(3) ×2	*M*1–O2	2.398(3) ×3
P1–O3	1.537(5) ×2	*M*1–O2	2.785(3) ×3
P1–O3A	1.562(12) ×2	*M*1–O3	2.90(2) ×3
<P1–O>	1.55		
		*M*2–O3	2.662(4) ×2
*M*2A–Cl	2.87(3)	*M*2–O2	2.694(3) ×2
*M*2A–F1	2.390(16)	*M*2–O3A	2.692(12) ×2
*M*2A–F1	2.491(16)	*M*2–O1	3.039(7)
*M*2A–F	2.50(2)	*M*2–F	2.667(8) ×2
*M*2A–F	2.73(2)	*M*2–F1	2.490(4) ×2
*M*2A–O3	2.42(3)	*M*2–*M*2A	0.30(4)
*M*2A–O3	2.74(2)		
*M*2A–O3A	2.42(4)	Cl–F	0.84(2) ×2
*M*2A–O3A	2.63(2)	Cl–F1	1.45(2) ×2
*M*2A–O3A	2.775(11)		
*M*2A–O3A	2.86(2)	F–F	1.67(4)
*M*2A–O2	2.722(14)	F–F1	0.616(17)
*M*2A–O2	2.778(18)	F–F1	1.48(4)
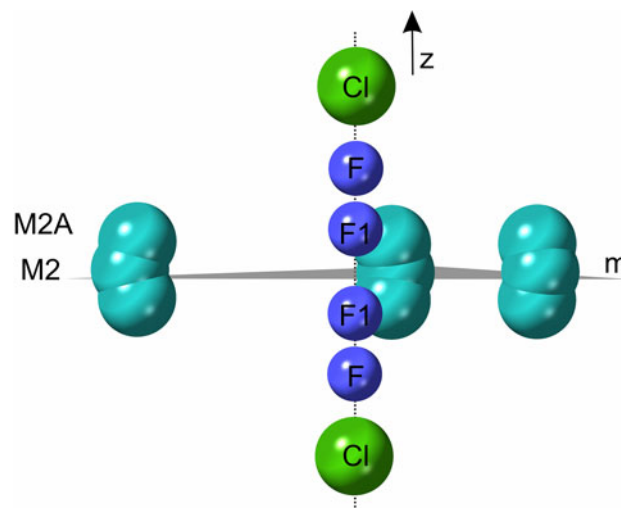
Figure 7. Anion positions (*c*-axis vertical) with respect to the mirror plane in fluoralforsite. Atoms are represented as thermal ellipsoids. Colour code as in Fig. 5. The dark grey triangle represents the mirror plane. The dotted line indicates *c*-axis.

cation. Nevertheless, the chemical analyses indicate a slight dominance of barium at the *M*1 sites, which may induce local disorder.

In addition, the hypothetical cations ordering at *M*1 sites would also affect the O1 site, which, similarly to O2, lies on the mirror plane. The refined values of O1 atomic displacement parameters (Table 5) indicate an elongation along the *c*-axis, even though the amount of the displacement is less pronounced than that observed for O2 (Table 5). Apart from O2 and O1, additional sites show a displacement along the *c*-axis: *M*2, which is refined as a split position between *M*2 and *M*2A; and fluorine, which is also modelled by two sites, F and F1, 0.61 Å apart along *c*. (Table 4). The splitting of *M*2 was not observed in alforsite or in the synthetic counterpart, though it has been noticed in the apatite structure, where the Cl anion is shifted towards the mirror plane (Sudarsanan and Young, 1978; Hughes *et al.*, 1990; Hughes and Rakovan, 2002). The *M*2 displacement in fluoralforsite might be triggered by the presence of Cl. This would also justify greater displacement of O2 with respect to O1: the *M*2–O2 distance is shorter (2.78 Å) than *M*2–O1 (3.04 Å). The re-arrangement of *M*2 has a stronger effect on the oxygen at O2 and O3 with respect to that at O1.

It is also conceivable that the splitting of the *M*2 position results from two overlapping effects, that is: (1) the local order at *M*1 sites and the subsequent split of O2, O3 and O1; and (2) the disorder of anions along [001].

Table 7. Distances (Å) between anions in the channels of fluoralforsite structure. Grey colour indicates too-short distances for simultaneous occupancy of both sites.*

		Mirror-related sites with mirror plane at $z = \frac{3}{4}$					
		Cl$_a$	F$_a$	F1$_a$	F1$_b$	F$_b$	Cl$_b$
	Cl$_a$	3.769	2.932	2.314	1.455	0.837	—
Mirror-related	F$_a$	4.606	3.769	3.151	2.292	1.673	0.837
sites with mirror	F1$_a$	5.224	4.387	3.769	2.910	2.292	1.455
plane at $z = \frac{1}{4}$	F1$_b$	6.083	5.247	4.628	3.769	3.151	2.314
	F$_b$	6.701	5.865	5.247	4.387	3.769	2.932
	Cl$_b$	7.538	6.701	6.083	5.224	4.606	3.769

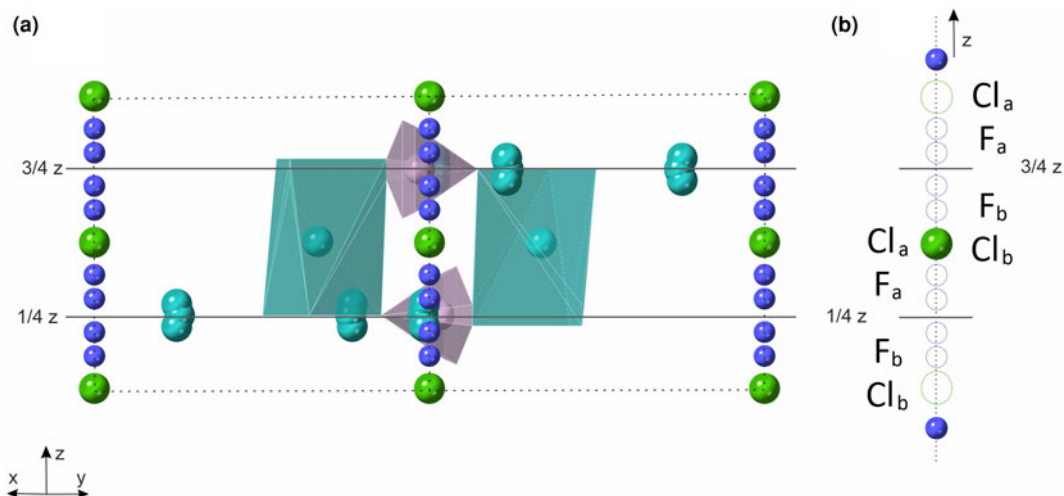*Note: 'b' subscript – below mirror plane, 'a' subscript – above mirror plane.

Figure 8. (a) Unit cell (dotted line) of fluoralforsite projected along [110] with the mirror planes at ¼ z and ¾ z marked by solid grey lines. (b) Possible F⁻ and Cl⁻ arrangement along the channel parallel to [001]. Colour code as in Fig. 5. 'b' subscript – below mirror plane, 'a' subscript – above mirror plane. The dotted line indicates the c-axis. Drawn using *CrystalMaker®* software.

Compared to fluorapatite, F⁻ is displaced off the mirror plane in fluoralforsite, forming two symmetrical partially-occupied equivalent sites, corresponding to the hydroxyl group in hydroxylapatite (Mathew *et al.*, 1979; Hughes *et al.*, 2018; Hazrah and Antao, 2022). In the hexagonal apatite structure, the position of the anionic sites depends on the size of the anions and *M*2 cations (Hata *et al.*, 1979; Hughes *et al.*, 1990). Therefore, the splitting of the F site with respect to fluorapatite can be considered a result of the larger Ba size compared to Ca. However, F anions are displaced ~0.74 Å (considering an average position between F and F1 sites) below or above the mirror plane in fluoralforsite, whereas in synthetic $Ba_5(PO_4)_3F$, the displacement is significantly smaller (~0.24 Å). The greater distance of F anions from the mirror plane is ascribed to the minor presence of the hydroxyl group.

Previous studies show that complete disordering along anion columns is unrealistic due to contacts being too short with neighbouring anions (Hughes *et al.*, 1989, 1990; Biagioni *et al.*, 2017; Pieczka *et al.*, 2018). The anion position in hexagonal ternary apatites depends on the adjacent anionic sites in the channel (Hughes and Rakovan, 2002). Therefore, the ordering arrangement of anions is required within individual columns, but the disordering of columns throughout the apatite structure allows the hexagonal symmetry to be maintained (Hughes *et al.*, 1989; Hughes and Rakovan, 2002; Biagioni *et al.*, 2017). In fluoralforsite, the F sites, located above and below the mirror plane and Cl site cannot be occupied simultaneously (Table 7, Fig. 8). The arrangement of F and Cl can be as follows: F (above the mirror plane) − Cl − F (below mirror plane; Fig 7). The adjacency of two chlorines is implausible due to the low content in the structure.

Considering the chlorine and hydroxyl group content, the sample studied can be regarded as a ternary barium phosphate. An ordered arrangement of Ba/Ca at the *M*1 site is very likely to occur within individual columns, however adjacent columns are disordered with respect to each other, similar to the anionic columns of hexagonal apatites (Hughes *et al.*, 1989; Hughes and Rakovan, 2002). The ordering of cations at the *M*1 position is characteristic of belovite-group minerals, where the *M*1 site is split into *M*1 and *M*1' and the symmetry is lowered to $P6_3$ or $P\bar{3}$ (Pasero *et al.*, 2010). In our study, the chemical analyses and single-crystal X-ray diffraction data indicate the dominance of barium at *M*2 sites

and slight occupancy at the *M*1 site, enabling the sample investigated to be included in the apatite group. A similar issue has been investigated by Biagioni *et al.* (2019) for hydroxylhedyphane $Ca_2Pb_3(AsO_4)_3(OH)$ ($P\bar{3}$), in which the *M*1 site splits into *M*1 and *M*1' but with Ca as the dominant cation at both sites. On that basis the authors classified the mineral as belonging to the hedyphane group and suggested the possible occurrence of intermediate phases between hedyphane and belovite groups (Biagioni *et al.*, 2019). Likewise, the data provided here about the new mineral species − fluoralforsite indicate the possibility of the existence of intermediate phases between belovite and apatite groups and suggest a possible new member of the belovite group with end-member formula $BaCaBa_3(PO_4)_3F$ and symmetry $P6_3$ or $P\bar{3}$.

Genesis of fluoralforsite

Fluoralforsite is a novel barium mineral from rankinite-rich paralavas that occurs in intergranular space and enclaves. Studies on the pyrometamorphic rocks of the Hatrurim Basin have distinguished two main types of enclaves, ferrite and silicate–phosphate. The origin of them is related to the crystallisation of residual melt between large crystals of paralava rock-forming minerals. The first type is dominated by minerals such as khesinite, Fe-spinels (magnetite, magnesioferrite, trevorite and cuprospinel), harmunite, barioferrite, perovskite and a nataliakulikite-like phase (Galuskina *et al.*, 2017b; Krzątała *et al.*, 2018). Walstromite or zadovite minerals can be dominant in the second type − silicate–phosphate enclaves enriched in elements such as Ba, K, V, Nb, U and Sr. The walstromite-type enclaves, which co-occur with wollastonite and cuspidine have been described by Krzątała *et al.* (2020). Fluoralforsite was found in zadovite enclaves, which are usually associated with fluorapatite (Fig. 3). The formation of a Ba-bearing enclave is a result of non-equilibrium between the primary minerals and residual melt, indicated by the melting of fluorapatite rims (Fig. 3d). It led to the enrichment of the silica-rich residual melt in phosphorus. Consequently, zadovite and fluoralforsite were formed at the final crystallisation stage of the paralava.

Fluoralforsite is a novel barium mineral from rankinite-rich paralavas that occurs in intergranular space and enclaves. Studies

on the pyrometamorphic rocks of the Hatrurim Basin have distinguished two main types of enclaves, ferrite and silicate–phosphate. The origin of them is related to the crystallisation of residual melt between large crystals of paralava rock-forming minerals. The first type is dominated by minerals such as khesinite, Fe-spinels (magnetite, magnesioferrite, trevorite and cuprospinel), harmunite, bario ferrite, perovskite and a nataliakulikite-like phase (Galuskina *et al.*, 2017b; Krzątała *et al.*, 2018). Walstromite or zadovite minerals can be dominant in the second type − silicate–phosphate enclaves enriched in elements such as Ba, K, V, Nb, U and Sr. The walstromite-type enclaves, which co-occur with wollastonite and cuspidine have been described by Krzątała *et al.* (2020). Fluoralforsite was found in zadovite enclaves, which are usually associated with fluorapatite (Fig. 3). The formation of a Ba-bearing enclave is a result of non-equilibrium between the primary minerals and residual melt, indicated by the melting of fluorapatite rims (Fig. 3d). It led to the enrichment of the silica-rich residual melt in phosphorus. Consequently, zadovite and fluoralforsite were formed at the final crystallisation stage of the paralava.

In summary, rock-forming minerals such as melilites of the alumoåkermanite–gehlenite series, Ti-rich andradite, fluorapatite and calcium silicates such as rankinite and/or wollastonite crystallised from the primary melt. Subsequently, residual fluid/melt rich in halides, mainly fluorine and chlorine and incompatible elements reacted with early-formed minerals. These changes enhanced the mineral variety and contributed to the formation of new minerals such as fluoralforsite. It is noteworthy that the mineralisation of both ferrite and silicate–phosphate enclave types originate from similar processes − high-temperature alteration between pre-existing pyrometamorphic minerals and residual melt (Galuskina *et al.*, 2017b; Galuskin *et al.*, 2016, 2017).

References

Baikie T., Schreyer M., Wei F., Herrin J.S., Ferraris C., Brink F., Topolska J., Piltz R.O., Price J. and White T.J. (2014) The influence of stereochemically active lone-pair electrons on crystal symmetry and twist angles in lead apatite-2H type structures. *Mineralogical Magazine*, **78**, 325–345.

Biagioni C., Bosi F., Hålenius U. and Pasero M. (2017) The crystal structure of turneaureite, Ca₅(AsO₄)₃Cl, the arsenate analog of chlorapatite, and its relationships with the arsenate apatites johnbaumite and svabite. *American Mineralogist*, **102**, 1981–1986.

Biagioni C., Hålenius U., Pasero M., Karlsson A. and Bosi F. (2019) Hydroxylhedyphane, Ca₂Pb₃(AsO₄)₃(OH), a new member of the apatite supergroup from Långban, Sweden. *European Journal of Mineralogy*, **31**, 1015–1024.

Britvin S.N., Murashko M.N., Vapnik Y., Polekhovsky Y.S. and Krivovichev S.V. (2015) Earth's Phosphides in Levant and insights into the source of Archean prebiotic phosphorus. *Scientific Reports*, **5**, 8355.

Burg A., Starinsky A., Bartov Y. and Kolodny Y. (1991) Geology of the Hatrurim Formation ("Mottled Zone") in the Hatrurim basin. *Israel Journal of Earth Sciences*, **40**, 107–124.

Comodi P., Liu Y., Stoppa F. and Woolley A.R. (1999) A multi-method analysis of Si-, S- and *REE*-rich apatite from a new find of kalsilite-bearing leucitite (Abruzzi, Italy). *Mineralogical Magazine*, **63**, 661–672.

Farrugia L.J. (2012) *WinGX* and *ORTEP for Windows*: an update. *Journal of Applied Crystallography*, **45**, 849–854.

Friis H., Balić-Žunić T., Pekov I.V. and Petersen O.V. (2004) Kuannersuite-(Ce), Ba₆Na₂REE₂(PO₄)₆FCl, a new member of the apatite group, from the Ilimaussaq alkaline complex, South Greenland. *The Canadian Mineralogist*, **42**, 95–106.

Frost R.L., Palmer S.J., Čejka J., Sejkora J., Plášil J., Bahfenne S. and Keeffe E.C. (2011) A Raman spectroscopic study of the different vanadate groups in solid-state compounds-model case: mineral phases vésigniéite [BaCu₃(VO₄)₂(OH)₂] and volborthite [Cu₃V₂O₇(OH)₂·2H₂O]. *Journal of Raman Spectroscopy*, **42**, 1701–1710.

Galuskin E.V., Gfeller F., Armbruster T., Galuskina I.O., Vapnik Y., Murashko M., Włodyka R. and Dzierżanowski P. (2015a) New minerals with a modular structure derived from hatrurite from the pyrometamorphic Hatrurim Complex. Part I. Nabimusaite, KCa₁₂(SiO₄)₄(SO₄)₂O₂F, from larnite rocks of Jabel Harmun, Palestinian Autonomy, Israel. *Mineralogical Magazine*, **79**, 1061–1072.

Galuskin E.V., Gfeller F., Galuskina I.O., Pakhomova A., Armbruster T., Vapnik Y., Włodyka R., Dzierżanowski P. and Murashko M. (2015b) New minerals with a modular structure derived from hatrurite from the pyrometamorphic Hatrurim Complex. Part II. Zadovite, BaCa₆[(SiO₄)(PO₄)](PO₄)₂F and aradite, BaCa₆[(SiO₄)(VO₄)](VO₄)₂F, from paralavas of the Hatrurim Basin, Negev Desert, Israel. *Mineralogical Magazine*, **79**, 1073–1087.

Galuskin E.V., Galuskina I.O., Gfeller F., Krüger B., Kusz J., Vapnik Y., Dulski M. and Dzierżanowski P. (2016) Silicocarnotite, Ca₅[(SiO₄)(PO₄)](PO₄), a new „old" mineral from the Negev Desert, Israel, and the ternesite–silicocarnotite solid solution: indicators of high-temperature alteration of pyrometamorphic rocks of the Hatrurim Complex, Southern Levant. *European Journal of Mineralogy*, **28**, 105–123.

Galuskin E.V., Gfeller F., Galuskina I.O., Armbruster T., Krzątała A., Vapnik Y., Kusz J., Dulski M., Gardocki M., Gurbanov A.G. and Dzierżanowski P. (2017) New minerals with a modular structure derived from hatrurite from the pyrometamorphic rocks. Part III. Gazeevite, BaCa₆(SiO₄)₂(SO₄)₂O, from Israel and the Palestine Autonomy, South Levant, and from South Ossetia, Greater Caucasus. *Mineralogical Magazine*, **81**, 499–513.

Galuskina I.O., Vapnik Y., Lazic B., Armbruster T., Murashko M. and Galuskin E.V. (2014) Harmunite CaFe₂O₄: A new mineral from the Jabel Harmun, West Bank, Palestinian Autonomy, Israel. *American Mineralogist*, **99**, 965–975.

Galuskina I.O., Galuskin E.V., Vapnik Y., Prusik K., Stasiak M., Dzierżanowski P. and Murashko M. (2017a) Gurimite, Ba₃(VO₄)₂ and hexacelsian, BaAl₂Si₂O₈ − two new minerals from schorlomite-rich paralava of the Hatrurim Complex, Negev Desert, Israel. *Mineralogical Magazine*, **81**, 1009–1019.

Galuskina I.O., Galuskin E.V., Pakhomova A.S., Widmer R., Armbruster T., Krüger B., Grew E.S., Vapnik Y., Dzierażanowski P. and Murashko M. (2017b) Khesinite, Ca₄Mg₂Fe₁₀³⁺O₄[(Fe₁₀³⁺Si₂)O₃₆], a new rhönite-group (sapphirine supergroup) mineral from the Negev Desert, Israel − natural analogue of the SFCA phase. *European Journal of Mineralogy*, **29**, 101–116.

Geller Y.I., Burg A., Halicz L. and Kolodny Y. (2012) System closure during the combustion metamorphic "Mottled Zone" event, Israel. *Chemical Geology*, **334**, 25–36.

Gfeller F., Widmer R., Krüger B., Galuskin E.V., Galuskina I.O. and Armbruster T. (2015) The crystal structure of flamite and its relation to Ca₂SiO₄ polymorphs and nagelschmidtite. *European Journal of Mineralogy*, **27**, 755–769.

Gross S. (1977) The mineralogy of the Hatrurim Formation, Israel. *Geological Survey of Israel Bulletin*, 70.

Hata M., Marumo F., Iwai S. and Aoki H. (1979) Structure of barium chlorapatite. *Acta Crystallographica*, **B35**, 2382–2384.

Hatert F., Mills S.J., Pasero M. and Williams P.A. (2013) CNMNC guidelines for the use of suffixes and prefixes in mineral nomenclature, and for the preservation of historical names. *European Journal of Mineralogy*, **25**, 113–115.

Hawthorne F.C., Krivovichev S.V. and Burns P.C. (2000) The crystal chemistry of sulfate minerals. Pp. 1–112 in: *Sulfate Minerals: Crystallography, Geochemistry, and Environmental Significance* (C.N. Alpers, J.L. Jambor

and D.K. Nordstrom, editors). Reviews in Mineralogy and Geochemistry, **40**. Mineralogical Society of America and the Geochemical Society, Washington, D.C.

Hazrah K. and Antao S. (2022) Apatite, $Ca_{10}(PO_4)_6(OH,F,Cl)_2$: structural variations, natural solid solutions, intergrowths, and zoning. *Minerals*, **12**, 527.

Henderson C.M.B., Bell A.M.T., Charnock J.M., Knight K.S., Wendlandt R.F., Plant D.A. and Harrison W.J. (2009) Synchrotron X-ray absorption spectroscopy and X-ray powder diffraction studies of the structure of johnbaumite $[Ca_{10}(AsO_4)_6(OH,F)_2]$ and synthetic Pb-, Sr- and Ba-arsenate apatites and some comments on the crystal chemistry of the apatite structure type in general. *Mineralogical Magazine*, **73**, 433−455.

Hughes J.M. and Rakovan J. (2002) The crystal structure of apatite, $Ca_5(PO_4)_3(F,OH,Cl)$. Pp. 1−12 in: *Phosphates* (M.L. Kohn, J. Rakovan, and J.M. Hughes, editors). Reviews in Mineralogy and Geochemistry, **48**. Mineralogical Society of America and the Geochemical Society, Washington, D.C.

Hughes J.M., Cameron M. and Crowley K.D. (1989) Structural variations in natural F, OH, and Cl apatites. *American Mineralogist*, **74**, 870−876.

Hughes J.M., Cameron M. and Crowley K.D. (1990) Crystal structures of natural ternary apatites: Solid Solution in the $Ca_5(PO_4)_3X$ (X: F, OH, Cl) system. *American Mineralogist*, **75**, 295−304.

Hughes J.M., Harlov D. and Rakovan J.F. (2018) Structural variations along the apatite F-OH join. *American Mineralogist*, **103**, 1981−1987.

Juroszek R., Galuskina I.O., Krüger B., Krüger H., Vapnik Y. and Galuskin E.V. (2022) Mazorite, IMA 2022-022. CNMNC Newsletter 68. *Mineralogical Magazine*, **86**, 856.

Klevtsova R.F. (1965) The crystal structure of strontium-apatite. *Journal of Structural Chemistry*, **5**, 2, 292−294.

Krząta≥a A., Panikorovskii T.L., Galuskina I.O. and Galuskin E.V. (2018) Dynamic Disorder of Fe^{3+} Ions in the Crystal Structure of Natural Barioferrite. *Minerals*, **8**, 340.

Krząta≥a A., Krüger B., Galuskina I., Vapnik Y. and Galuskin E. (2020) Walstromite, $BaCa_2(Si_3O_9)$, from Rankinite Paralava within Gehlenite Hornfels of the Hatrurim Basin, Negev Desert, Israel. *Minerals*, **10**, 407.

Krząta≥a A., Krüger B., Galuskina I., Vapnik Y. and Galuskin E. (2022) Bennesherite, $Ba_2Fe^{2+}Si_2O_7$: A new melilite group mineral from the Hatrurim Basin, Negev Desert, Israel. *American Mineralogist*, **107**, 138−146.

Levitt S.R. and Condrate R.A., Sr. (1970) The vibrational spectra of lead apatites. *American Mineralogist*, **55**, 1562−1575.

Litasov K.D. and Podgornykh N.M. (2017) Raman spectroscopy of various phosphate minerals and occurrence of tuite in the Elga IIE iron meteorite: Raman spectroscopy of various phosphate minerals. *Journal of Raman Spectroscopy*, **48**, 1518−1527.

Mathew M., Mayer I., Dickens J.B. and Schroeder L.W. (1979) Substitution in Barium-Fluoride Apatite: The Crystal Structures of $Ba_{10}(PO_4)_6F_2$, $Ba_6La_2Na_2(PO_4)_6F_2$ and $Ba_4Nd_3Na_3(PO_4)_6F_2$. *Journal of Solid State Chemistry*, **28**, 79−95.

Meegoda C., Bonner C.E., Loutts G., Stefanos S. and Miller G.E. (1999) Raman spectroscopic study of barium fluorapatite. *Journal of Luminescence*, **81**, 101−109.

Newberry N.G., Essene E.J. and Peacor D.R. (1981) Alforsite, a new member of the apatite group: the barium analogue of chlorapatite. *American Mineralogist*, **66**, 1050−1053.

Nishio-Hamane D., Ogoshi Y. and Minakawa T. (2012) Miyahisaite, $(Sr, Ca)_2Ba_3(PO_4)_3F$, a new mineral of the hedyphane group in the apatite supergroup from the Shimoharai mine, Oita Prefecture, Japan. *Journal of Mineralogical and Petrological Sciences*, **107**, 121−126.

Novikov I., Vapnik Y. and Safonova I. (2013) Mud volcano origin of the Mottled Zone, South Levant. *Geoscience Frontiers*, **4**, 597−619.

Nyfeler D. and Armbruster T. (1998) Silanol groups in minerals and inorganic compounds. *American Mineralogist*, **83**, 119−125.

Pasero M., Kampf A.R., Ferraris C., Pekov I.V., Rakovan J. and White T.J. (2010) Nomenclature of the apatite supergroup minerals. *European Journal of Mineralogy*, **22**, 163−179.

Pekov I.V., Britvin S.N., Zubkova N.V., Pushcharovsky D.Yu., Pasero M. and Merlino S. (2010) Stronadelphite, $Sr_5(PO_4)_3F$, a new apatite-group mineral. *European Journal of Mineralogy*, **22**, 869−874.

Pekov I.V., Zubkova N.V., Husdal T.A., Kononkova N.N., Agakhanov A.A., Zadov A.E. and Pushcharovsky D.Y. (2012) Carlgieseckeite-(Nd), $NaNdCa_3(PO_4)_3F$, a new belovite-group mineral species from the Ilimaussaq alkaline complex, South Greenland. *The Canadian Mineralogist*, **50**, 571−580.

Pieczka A., Biagioni C., Gołębiowska B., Jeleń P., Pasero M. and Sitarz M. (2018) Parafiniukite, $Ca_2Mn_3(PO_4)_3Cl$, a New Member of the Apatite Supergroup from the Szklary Pegmatite, Lower Silesia, Poland: Description and Crystal Structure. *Minerals*, **8**, 485.

Schulte A., Buchter S.C. and Chai B.H.T. (1995) Raman spectroscopy of fluorophosphate and fluorovanadate laser crystals. Pp. 34−42 in: *UV and Visible Lasers and Laser Crystal Growth* (R. Scheps and M.R. Kokta, editors). SPIE, San Jose, United States.

Sharygin V., Vapnik Y., Sokol E., Kamenetsky V. and Shagam R. (2006) Melt inclusions in minerals of schorlomite-rich veins of the Hatrurim Basin, Israel: composition and homogenization temperatures. *ACROFI I Program with Abstracts*, 189−192.

Sheldrick G.M. (2008) A short history of *SHELX*. *Acta Crystallographica*, **A64**, 112−122.

Sheldrick G.M. (2015) Crystal structure refinement with *SHELXL*. *Acta Crystallographica*, **C71**, 3−8.

Sudarsanan K. and Young R.A. (1978) Structural interactions of F, Cl and OH in apatites. *Acta Crystallographica*, **B34**, 1401−1407.

Vapnik Y., Sharygin V.V., Sokol E.V. and Shagam R. (2007) Paralavas in a combustion metamorphic complex Hatrurim Basin, Israel. Pp. 133−153 in: *Geology of Coal Fires. Case Studies from Around the World*. The Geological Society of America, Reviews in Engineering, Vol. **18**.

Warr L.N. (2021) IMA−CNMNC approved mineral symbols. *Mineralogical Magazine*, **85**, 291−320.